Materials Advances

ROYAL SOCIETY OF CHEMISTRY

PAPER

View Article Online
View Journal | View Issue

Cite this: *Mater. Adv.*, 2022, 3, 4015

Thermal stabilities of Mn-based active materials in combination with the ceramic electrolyte LATP for ASSB bulk cathodes†

Matthias Rumpel, *[a] Felix Nagler,[a] Lavinia Appold,[a] Werner Stracke,[a] Andreas Flegler,[a] Oliver Clemens [b] and Gerhard Sextl[a]

Ternary composite bulk cathodes consisting of particulate active material (AM), solid-state electrolyte (SSE) and electrical conductor are essential to achieve competitive ceramic all solid-sate batteries (ASSBs). Firmly bonded contacts between AM and SSE as well as between the SSE particles are required to obtain fast Li-ion transfer and, thus, a good electrochemical performance. Consequently, sintering processes are unavoidable. However, decomposition processes, the formation of mixed phases and interdiffusion can take place during high temperature annealing, so that non-conductive or electrochemically inactive phases can be formed, which significantly reduce the ASSB performance. Consequently, a thermally stable material combination needs to be found. By understanding the thermodynamical processes, the selection of components can be simplified or the heat treatment can be optimized. For that purpose, this study investigates the thermal stabilities of the three Mn-based AMs $LiMn_2O_4$ (LMO-s), $LiMnO_2$ (LMO-l) and $LiMnPO_4$ (LMP) in combination with the ceramic electrolyte $Li_{1.3}Al_{0.3}Ti_{1.7}(PO_4)_3$ (LATP). It can be demonstrated, that LMO-s and LMO-l already decompose below 500 °C due to reduction of the Mn transition metal and the formation of oxygen gas. It results in a porous multicomponent composite, which is unusable for the application in ASSBs. In contrast, the powder mixture of LMP and LATP is thermally stable up to 800 °C in argon atmosphere and shows a dense microstructure. The addition of Ag as electrical conductor to LMP and LATP does not have an impact on the thermal stability, so that this material combination is promising for further ASSB bulk cathode development.

Received 11th February 2022,
Accepted 1st April 2022

DOI: 10.1039/d2ma00158f

rsc.li/materials-advances

Introduction

All solid-state batteries (ASSB) promise higher energy densities, longer cycle life and higher safety than conventional liquid electrolyte Li-ion batteries. Suppression of dendrite growth and implementation of high voltage active materials as well as Li-metal anodes can theoretically be achieved by the replacement of the liquid electrolyte with a ceramic or glassy solid-state electrolyte. This leads to higher energy densities and a significantly higher safety, since the risks of leakage and flammability of the organic liquid electrolyte are eliminated.[1–8] First thin-film ASSBs based on glassy lithium phosphorus oxynitride (LIPON) impressively demonstrate the benefits of a solid-state electrolyte in combination with a Li-metal anode in terms of cycle life and cycle stability.[9] However, the thickness of the cathode active material layer is limited by its electrical and ionic conductivities to about 1 μm, so that high energy densities cannot be obtained. Furthermore, vacuum based sputter processes are usually used to manufacture thin-film ASSBs, which additionally results in high production costs. Consequently, particulate bulk cathodes of a few tens of micrometers consisting of active material (AM), solid-state electrolyte (SSE) and an electrical conductive component are in focus of further research towards competitive ASSBs with high energy densities.[1–3] The bulk cathode layer can be prepared by slurry preparation and roll-to-roll processes. High temperature processes are necessary for sintering and densification of the green body layer in order to maximize the electrochemically active grain to grain contact area and to enhance the Li-ion charge transfer due to the formation of firmly bonded contacts between SSE and AM particles as well as between SSE particles. However, heat treatment of these material combinations can cause side effects like interdiffusion, formation of mixed phases and decomposition,

[a] *Fraunhofer Institute for Silicate Research ISC, Neunerplatz 2, 97082 Wuerzburg, Germany. E-mail: matthias.rumpel@isc.fraunhofer.de*
[b] *University Stuttgart, Institute for Material Sciences, Chemical Materials Synthesis, Heisenbergstraße 3, 70569 Stuttgart, Germany*

† Electronic supplementary information (ESI) available. See https://doi.org/10.1039/d2ma00158f

which reduce significantly the cell performance, when the formation of non-conductive and electrochemical inactive mixed phases and the dissolution of the initial components take place.[10,11] In the field of thin-film ASSBs, the effect of interdiffusion during heat treatment of oxidic SSE thin-films, such as $Li_7La_3Zr_2O_{12}$ (LLZO) or $Li_{1+x}Al_xTi_{2-x}(PO_4)_3$ (LATP), in combination with AM thin-films, such as $LiCoO_2$ or $LiCoPO_4$, is well reported.[12,13] Sastre *et al.* reported a significant decrease in capacity due to mixed phase formation and interdiffusion during crystallization of LLZO on top of $LiCoO_2$ thin-films.[12] Considering the LATP and $LiCoPO_4$ combination, Hofmann *et al.* showed the interdiffusion of Co and Ti elements during crystallization of $LiCoPO_4$ thin-films on top of LATP.[13] However, since the thicknesses of the applied layers are <1 μm, the mixed phases are below the resolution limit of common X-ray diffraction techniques. Consequently, the investigation of annealed powder mixtures *via* X-ray powder diffraction spectroscopy gives a deeper insight in the mixed phase formation. Miara *et al.*, for instance, tested powder mixtures of three spinel AM ($LiCoMnO_4$, $LiNi_{0.5}Mn_{1.5}O_4$ and $LiFe_{0.5}Mn_{1.5}O_4$) in combination with LATP and LLZO on their thermal stability.[11] The authors could show that the formation of mixed phases starts between 600 °C and 700 °C for all material combinations. Gellert *et al.* demonstrated the highest thermal stability of powder mixtures for olivine AMs (*i.e.* $LiCoPO_4$) and LATP in comparison to material combinations of LATP and other AMs, such as $LiMn_2O_4$, $LiCoO_2$.[10]

The theoretical basis of interdiffusion, decomposition and mixed phase formation is the thermodynamical tendency to reach equilibrium condition for the chemical potentials of the elements due to diffusion along the concentration gradients within the multicomponent ceramic.[14–16] The chemical potential and the ability of interdiffusion of these elements mainly differ by their oxidation states, the ionic radii, chemical affinity and the lattice structure type of the host material.[14]

On basis of this thermodynamical consideration and previous results, this study takes a deeper look into the mixed phase formation and reaction mechanisms of LATP in combination with the three Mn-based AMs: $LiMn_2O_4$ (LMO-s), $LiMnO_2$ (LMO-l) and $LiMnPO_4$ (LMP). They represent the three common AM lattice structure types: spinel, layered and olivine, respectively.[17,18] Additionally, the valances of Mn in these lattice structures differ. The oxidation states of Mn are 3+ and 4+ for LMO-s, 3+ for LMO-l and 2+ for LMP. One important characteristic of the olivine LMP is the polyanion PO_4^{3-}, which has a strong covalent bonding between P and O. As a result, oxygen loss during overcharging is not observable, which is in contrast to the spinel and layered oxides.[17–20] LATP crystallize in a NASICON structure type with the oxidation state 3+ for Al und 4+ for Ti,[21] so that different starting conditions for the thermodynamic consideration are given for the three material combinations. The systematic comparison of these powder mixtures elucidates the differences in the reaction processes and mixed phase formations during sintering and reveals that LMP has a high thermal stability in combination with LATP. Furthermore, it can be shown that the addition of silver (Ag) particles as an electrical conductor to the LMP + LATP powder mixture has also a high thermal stability, so that this material combination can be a promising starting point for further investigations on ternary bulk cathodes for ASSBs.

Experimental

Powder preparation

$Li_{1.3}Al_{0.3}Ti_{1.7}(PO_4)_3$ (LATP), $LiMnPO_4$ (LMP) and $LiMn_2O_4$ (LMO-s) powders were synthesized *via* sol–gel routes. $LiMnO_2$ powder (LMO-l, particle size: <1 μm) and nano particulate silver powder (Ag, particle size: 48-78 nm) were purchased from Sigma Aldrich® and Nanografi®, respectively.

For LATP stoichiometric amounts of lithium acetate dihydrate, alumina nitrate nonahydrate and ammonium dihydrogen phosphate were dissolved in a 1 : 1 mixture of ethanol and 1-methoxy-2-propanol, to which concentrated nitric acid was added. In a second vessel Ti(IV) butoxide was added to acetyl acetone and stirred for 30 min to obtain a complete complex formation. Afterwards, the two solutions were mixed and stirred for further 30 min. The solution was dried overnight and the obtained amorphous powder was then crystallized at 800 °C for 5 h. Finally, the crystallized LATP powder was ball-milled at 400 rpm for 40 min.

LMP was synthesized by dissolving stoichiometric amounts of lithium acetate dihydrate, manganese(II) acetate tetrahydrate and ammonium dihydrogen phosphate in a 1 : 1 mixture of ethanol and 1-methoxy-2-propanol with additional concentrated nitric acid. The solution was stirred for 30 min and dried overnight. The amorphous powder was crystallized at 600 °C for 5 h and then ball-milled at 400 rpm for 40 min.

The LMO-s synthesis was performed by dissolving stoichiometric amounts of lithium acetylacetonate and manganese(II) acetate tetrahydrate in ethanol. After stirring for 30 min, the solution was dried overnight and crystallized at 600 °C for 5 h. The obtained crystalline LMO-s powder was ball-milled at 400 rpm for 40 min.

All preparation conditions were specifically chosen to obtain particle sizes below 1 μm and a similar particle size distribution, so that a homogenous particle distribution of the two components in the powder mixtures can be realized. SEM images (Fig. S1, ESI†) and the characterization of the starting powders (Fig. S2) can be found in the ESI.†

Powder mixtures and pellet preparation

Powder mixtures of 1 : 1 vol% of LATP and the various AMs were mixed in a mortar. The ratio of 1 : 1 vol% was chosen to maximize the interfaces between the two components in order to realize more accurate measurements of the thermal stabilities. In case of the LMP + LATP + Ag powder mixture the ratio was 1 : 1 : 1 vol%. Pellets of 0.25 g of these powder mixtures were pressed with 90 kN, which result in pellets with a thickness of 0.7 mm and a diameter of 14.85 mm.

Analyses of the thermal stabilities of the powder mixtures

High-temperature X-ray diffraction spectroscopy (HT-XRD) measurements were performed on a Bruker D8 advance

diffractometer with Cu K_α radiation between 14° and 54° 2θ. A Bragg–Brentano geometry was used. A high-temperature sample holder chamber (Anton Paar®) with controlled argon atmosphere was used inside the diffractometer. The temperature profile of the chamber was calibrated by using a defined MgO sample. The produced pellets of the powder mixtures were placed inside the chamber and heated up with 3 K min^{-1}. The first XRD scan was performed at 500 °C. During the 15 min XRD scan the temperature were kept constant. Afterwards, the heating rate was still 3 K min^{-1} and XRD scans were performed every 25 °C. The maximum temperature was hold for 1 h followed by a cooling process to 500 °C with 3 K min^{-1} and XRD scans every 25 °C. The maximum temperature was determined beforehand *via* a form integrity test. The maximum temperatures without deformation of the pellets are 900 °C for LMO-s + LATP, 1000 °C for LMO-l + LATP and 800 °C for LMP + LATP.

The XRD diffractograms were analysed *via* Rietveld refinement using the TOPAS V6 software (Bruker®) in order to obtain the phase fractions of the different components. Only the lattice parameters and crystalline size parameters were refined.

The differential scanning calorimetry and thermogravimetric analysis (DSC–TG) measurements were performed by using a Netzsch STA 449 C Jupiter set up. 20 mg of the respective powder mixture was heated up to 1000 °C in an alumina crucible with a heating rate of 10 K min^{-1} in argon atmosphere. Evaporation products were analyzed in a Netzsch MS 403 C Aeolos mass spectrometer (MS).

Scanning electron microscopy incl. energy dispersive X-ray analysis (SEM/EDS) were performed on polished cross sections of respective pellets, which were annealed in argon atmosphere at 800 °C for 2 h with a heating rate of 5 K min^{-1}. Cross sections were prepared by polishing one edge of the pellets with a HITACHI IM4000 ion milling system. A ZEISS AURIGA 60 microscope was used to obtain the SEM images and the EDS spectra were measured by means of the AMETEK EDAX Octane Elect Plus analytical system.

Results

Thermal stability of the LMO-s and LATP powder mixture

The phase fractions of the LMO-s + LATP pellet were obtained *via* HT-XRD and subsequent Rietveld refinement and are plotted in Fig. 1 as a function of the annealing temperature. A selection of the corresponding XRD diffractograms incl. the Rietveld fittings can be found in the ESI† (Fig. S3). The amounts of the starting powders LMO-s and LATP are already reduced at 500 °C. LMO-s intrinsically decomposes to high amounts of Mn_3O_4 and low amounts of Mn_2O_3 and vanishes at 650 °C. This decomposition goes along with the reduction of the Mn transition metal from Mn^{3+} and Mn^{4+} (LMO-s) to Mn^{2+} and Mn^{3+} (Mn_3O_4) or Mn^{3+} (Mn_2O_3). LATP starts also to intrinsically decompose to Li_3PO_4 and TiO_2 below 500 °C and to $LiTiOPO_4$ at 650 °C, until the complete decomposition is finished at 800 °C. The first reaction product (low amounts of $Mn_2P_2O_7$) of LMO-s and LATP can be detected at 500 °C. Afterwards, the decomposition products of LMO-s and LATP are the educts of subsequent reactions. For instance, LMP starts to form at 600 °C and significantly increases to 35 wt% at 850 °C. Further reaction products are $MnTiO_3$ and $Li(Mn,Ti)_2O_4$. The formation of $MnTiO_3$ can be detected at 725 °C and is followed by a strong increase to 20 wt% up to 900 °C. Low amounts of $Li(Mn,Ti)_2O_4$ are formed at 875 °C. These reactions go along with the vanishing of Mn_2O_3 at 800 °C and the significant decrease of Mn_3O_4 by about 32 wt% between 600 °C and 900 °C.

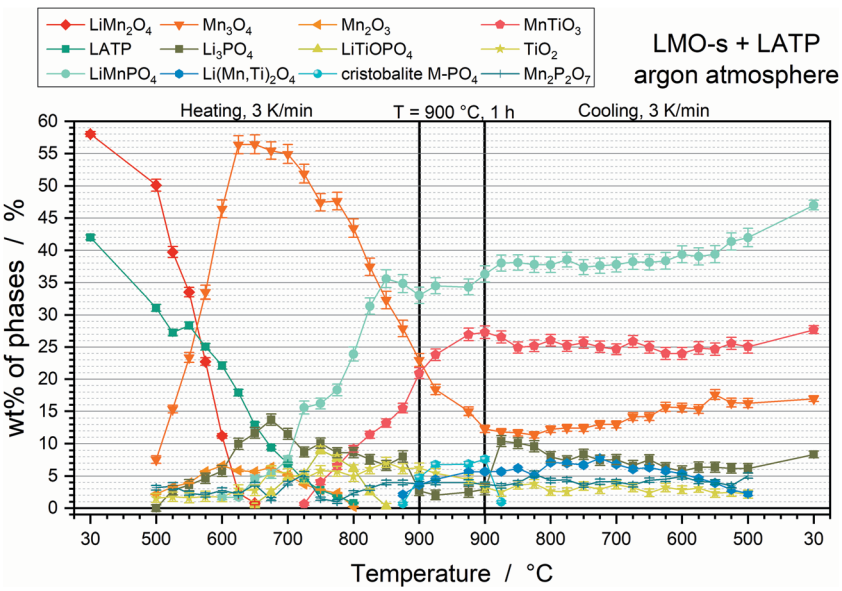

Fig. 1 Phase fractions in wt% of the crystalline phases obtained by Rietveld refinement of the LMO-s + LATP pellets as a function of the annealing temperature. Heating up to 900 °C with 3 K min^{-1}, holding step at 900 °C for 1 h, and afterwards cooling with 3 K min^{-1} to 30 °C.

Consequently, the formations of LMP and $MnTiO_3$ run in parallel to a further reduction of Mn, since the oxidation state of Mn is 2+ for LMP and $MnTiO_3$. In contrast, the oxidation state of Ti is 4+ in all Ti-containing species. During the holding step, another crystalline phase can be detected, which corresponds to a cristobalite M–PO_4 (M = Mn^{3+} or Ti^{3+}) phase. Since the amount of Mn_3O_4 shows a further decrease and the Ti-containing phases $MnTiO_3$ and $Li(Mn,Ti)_2O_4$ increase during the holding step, the M–PO_4 phase is most likely rich in $MnPO_4$. As the decrease of Mn_3O_4 (containing Mn^{3+}) phase together with the increase of $MnTiO_3$ (containing Mn^{2+}) is observable, it can be assumed that this cristobalite phase might contain Mn in its tetravalent oxidation state (Mn^{4+}) due to disproportionation. This would be also plausible since Mn^{3+} is Jahn–Teller active in $MnPO_4$ and thus unlikely to be stabilized in a tetrahedral site. The incorporation of Mn^{4+} into a cristobalite lattice would have to be accompanied with the integration of lower valent ions, *e.g.* Li^+ and Al^{3+}, which could be happening according to $Li_{x/2}Mn_xAl_{1-3x/2}PO_4$. However, the fact that the cristobalite phase is only a high temperature phase, since it cannot be stabilized by quenching, impedes a further detailed compositional analysis. It vanishes again at 850 °C during cooling. The phase fractions of the other phases remain quite constant during cooling, so that the final composition consists of 47 wt% LMP, 28 wt% $MnTiO_3$, 17 wt% Mn_3O_4 and 8 wt% Li_3PO_4.

Reduction of Mn during sintering is accompanied by oxidation of O^{2-} to O_2, which is detected *via* TG analysis and MS (Fig. 2a). The highest mass loss takes place between *ca.* 500 °C and 670 °C. The temperature derivation of the mass shows two rates for the oxygen formation, which correspond to two small endothermic peaks at 564 °C (Fig. 2a, P1) and 645 °C (Fig. 2a, P2) in the DSC curve. These reactions can be correlated to the Mn_3O_4 and Mn_2O_3 formation (Table 1). A lower degree of mass loss due to oxygen gassing occurs with two slopes at higher temperatures above *ca.* 670 °C. The corresponding two endothermic peaks at 803 °C (Fig. 2a, P3) and 862 °C (Fig. 2a, P4) can be correlated to the LMP and $MnTiO_3$ formations, since these reactions are accompanied by further Mn reduction. The formations of $Li(Mn,Ti)_2O_4$ and the cristobalite phase can be correlated to the endothermic peak at 916 °C (Fig. 2a, P5), however, since no further Mn reduction takes place, a further oxygen formation cannot be detected above 900 °C. The total mass loss due to oxygen gassing is 7.7%. A porous microstructure is formed due to the outgassing process (Fig. 2b). Grains of a few 100 nm, which appear in four different contrasts, can be detected. The EDS analysis of the four regions (Fig. 2c) is in good accordance with the HT-XRD measurements, since the contrasts can be correlated to Mn_3O_4

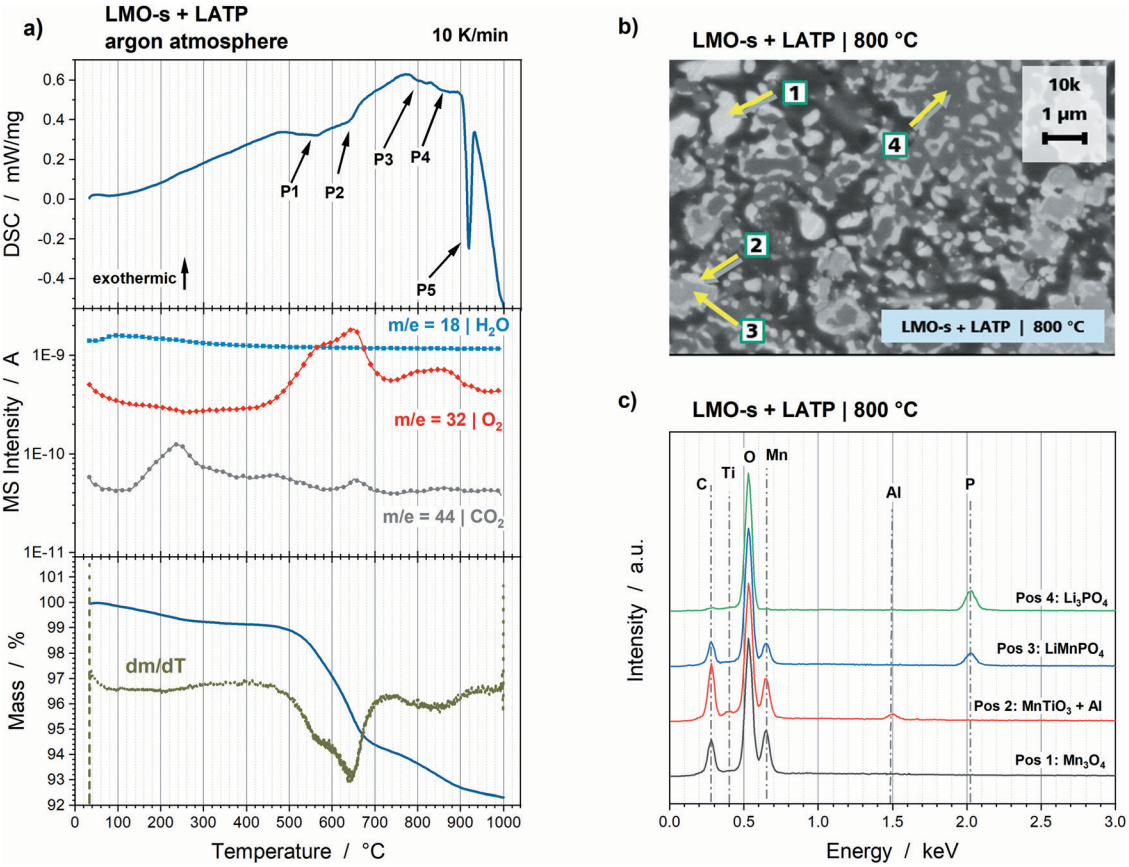

Fig. 2 (a) Results of DSC–TG and MS analyses of a 1 : 1 vol% LMO-s + LATP powder mixture measured in argon atmosphere with 10 K min^{-1}. (b) SEM cross section and (c) corresponding EDS analyses of the four positions marked in the SEM image of the LMO-s + LATP pellet sintered at 800 °C for 2 h at a heating rate of 5 K min^{-1} in argon atmosphere.

Table 1 Summary of the results and findings of the analyses of the thermal stability of LMO-s and LATP. DSC Peak positions: 564 °C (P1), 645 °C (P2), 803 °C (P3), 862 °C (P4) and 916 °C (P5)

Detected phases	Valence of transition metals	Temperature range and trend	Possible educts	Possible corres-ponding DSC Peaks	Expected oxygen formation and mass loss	Final composition (wt%)
$LiMn_2O_4$ (LMO-s)	Mn^{3+} and Mn^{4+}	Decrease already <500 °C, disappearance at 650 °C	—	—	—	—
$Li_{1.3}Al_{0.3}$-$Ti_{1.7}(PO_4)_3$ (LATP)	Al^{3+} and Ti^{4+}	Decrease already <500 °C, disappearance at 800 °C	—	—	—	—
Mn_2O_3	Mn^{3+}	Detectable between 500 °C and 800 °C	LMO-s	P1 and P2	Yes	—
Mn_3O_4	Mn^{2+} and Mn^{3+}	Formation already <500 °C strong increase up to 625 °C, afterwards steady decrease to 900 °C, during cooling constant	LMO-s	P1 and P2	Yes	17
Li_3PO_4	—	Detectable during heating and cooling	LATP	—	No	8
TiO_2	Ti^{4+}	Detectable during heating and cooling	LATP	—	No	—
$LiTiOPO_4$	Ti^{4+}	Detectable between 650 °C and 850 °C	LATP	—	No	—
$Mn_2P_2O_7$	Mn^{2+}	Detectable during heating and cooling	LMO-s and LATP	P1 and P2	Yes	—
$LiMnPO_4$	Mn^{2+}	Formation at 600 °C, strong increase to 850 °C, afterwards slight increase during cooling	LMO-s, Mn_2O_3, Mn_3O_4 and LATP	P3	Yes	47
$MnTiO_3$	Mn^{2+} and Ti^{4+} + Al^{3+} (dissolved)	Formation at 725 °C, strong increase to 900 °C, afterwards constant during cooling	Mn_2O_3, Mn_3O_4 and $LiTiOPO_4$, TiO_2	P4	Yes	28
$Li(Mn,Ti)_2O_4$	Mn^{3+} and Ti^{4+}	Formation at 875 °C, increase to 900 °C, afterwards decrease during cooling	Mn_3O_4 and TiO_2	P5	No	—
Cristobalite phase M–PO_4	n/a	Detectable during holding step at 900 °C	Mn_3O_4 and Li_3PO_4	P5	No	—

(Pos 1), $MnTiO_3$ (Pos 2), LMP (Pos 3) and Li_3PO_4 (Pos 4). Additionally, the EDS analysis reveals that Al is dissolved in $MnTiO_3$ lattice.

Conclusively, the LMO-s and LATP powder mixture is thermally unstable and decomposes already below 500 °C, which is accompanied by the reduction of Mn and oxygen gassing. The findings of this section are summarized in Table 1.

The quantitative analysis of the HT-XRD measurements *via* Rietveld refinement (Fig. S4, ESI†) show a comparable thermal

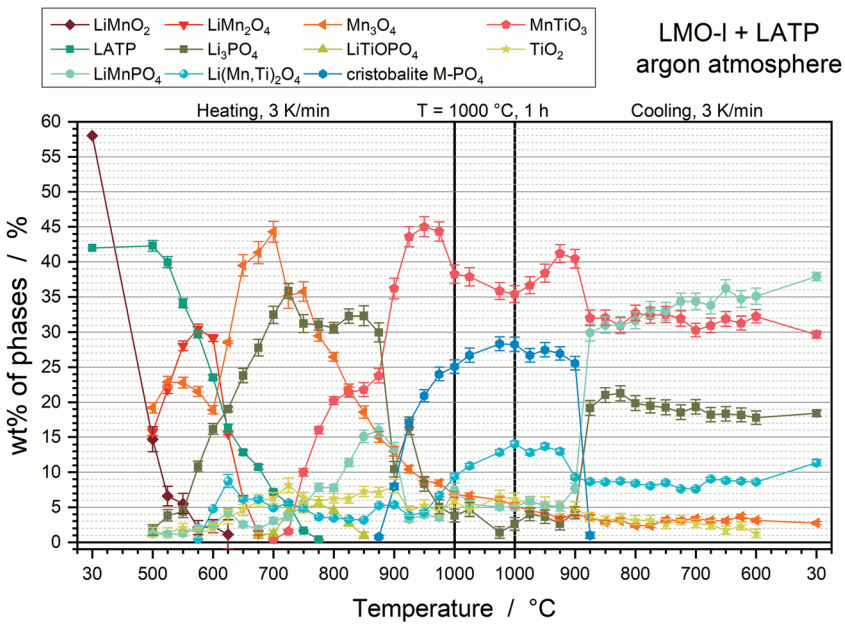

Fig. 3 Phase fractions in wt% of the crystalline phases obtained by Rietveld refinement of the LMO-I + LATP pellet as a function of the annealing temperature. Heating up to 1000 °C with 3 K min^{-1}, holding step at 1000 °C for 1 h, and afterwards cooling with 3 K min^{-1} to 30 °C.

behaviour of LMO-l and LMO-s in combination with LATP. The phase fractions of the LMO-l and LATP pellet show also intrinsical decompositions of the two components LMO-l and LATP (Fig. 3). LATP starts to decompose to Li_3PO_4 and TiO_2 at 525 °C and to $LiTiOPO_4$ at 675 °C. LATP is completely decomposed at 800 °C. LMO-l already decomposes to Mn_3O_4 and LMO-s below 500 °C. Since the oxidation states of Mn are 3+ for LMO-l, 2+ and 3+ for Mn_3O_4 as well as 3+ and 4+ for LMO-s, the decomposition is due to disproportionation. The tendency of LMO-l to transform to LMO-s has also been reported in literature for long time cycling of LMO-l in liquid electrolyte cells.[22–25] However, LMO-l and LMO-s disappear at 650 °C and 675 °C, respectively, which goes along with a strong increase of Mn_3O_4 up to 44 wt% at 700 °C. Consequently, the reduction of Mn seem to be once again one driving force for the decomposition. The decomposition products of LMO-l and LATP subsequently react to LMP at 500 °C, $Li(Mn,Ti)_2O_4$ at 575 °C and $MnTiO_3$ at 700 °C. The formation of $Li(Mn,Ti)_2O_4$ goes along with the vanishing of LMO-s. The increases in the amounts of LMP and $MnTiO_3$ are accompanied by a strong decrease of Mn_3O_4. Consequently, a further reduction of Mn takes place. As discussed before and in accordance with the LMO-s and LATP mixture, a high temperature cristobalite phase can be detected between 875 °C of heating and cooling, which goes along with a significant drop of Mn_3O_4, Li_3PO_4 and LMP during the holding step at 1000 °C. Because of the higher maximum temperature of 1000 °C, a tree times higher amount of the cristobalite phase M–PO_4 is formed for the LMO-l + LATP sample compared with the LMO-s + LATP sample. Below 875 °C during cooling, the cristobalite phase transforms again to Li_3PO_4 and LMP. Besides, $Li(Mn,Ti)_2O_4$ and $MnTiO_3$ decrease at 875 °C of cooling. Afterwards, the phase fractions remain constant and result in a final composition of 38 wt% $LiMnPO_4$, 30 wt% $MnTiO_3$, 18 wt% Li_3PO_4, 11 wt% $Li(Mn,Ti)_2O_4$ and 3 wt% Mn_3O_4.

Again DSC–TG and MS measurements show that endothermic peaks and the oxidation of O^{2-} to O_2, thus oxygen gassing, go along with the reduction reactions of the Mn-species detected in the HT-XRD measurements. The first endothermic peak at 662 °C (Fig. 4a, P1) is accompanied by a significant mass loss due to oxygen gassing, which can be correlated to the significant Mn_3O_4 formation to a total amount of 44 wt% (Fig. 3). The endothermic peaks at 707 °C (Fig. 4a, P2) and 816 °C (Fig. 4a, P3) can be correlated to the increase in LMP, $MnTiO_3$ or $Li(Mn,Ti)_2O_4$. A more specific correlation of the two peaks to one of these reactions is not possible. However, oxygen formation can be detected in the broad temperature range of the P3 peak, so that it is most likely connected to the reduction of

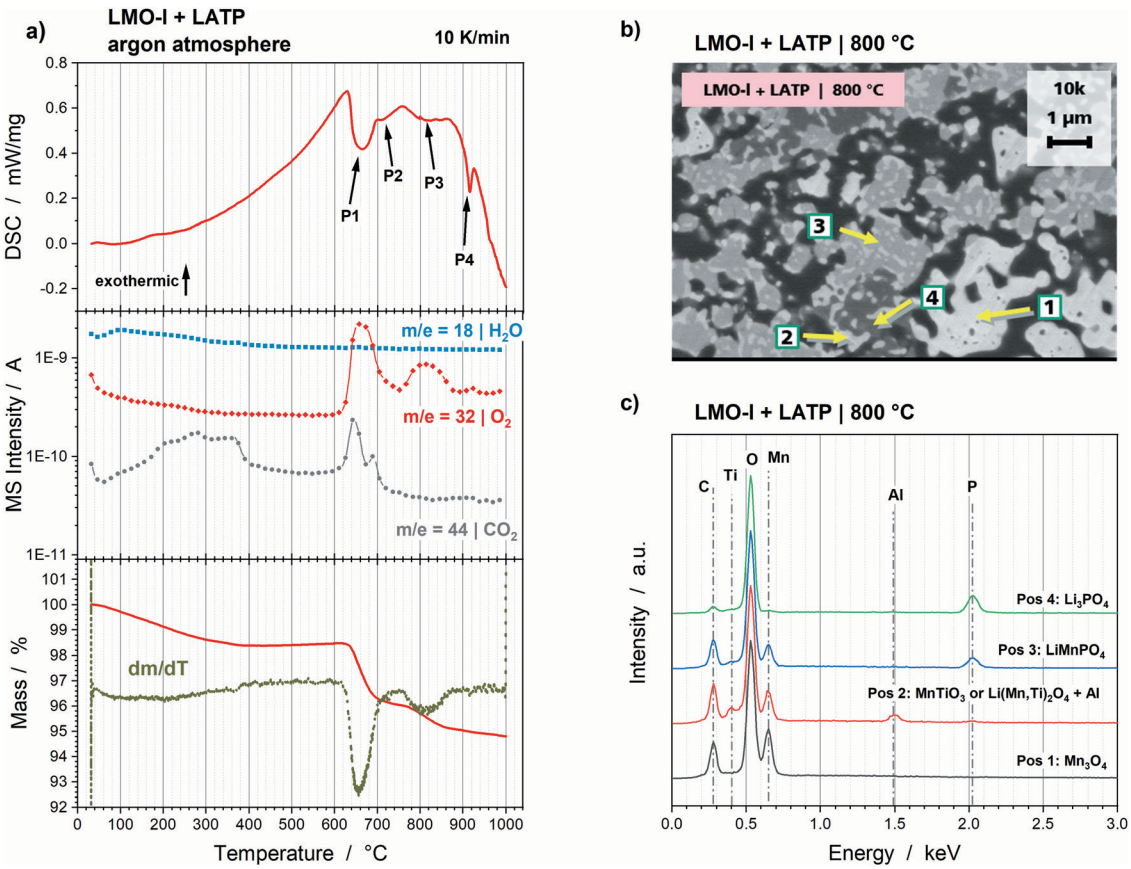

Fig. 4 (a) Results of DSC–TG and MS analyses of a 1 : 1 vol% LMO-l + LATP powder mixture measured in argon atmosphere with 10 K min^{-1}. (b) SEM cross section and (c) corresponding EDS analyses of the four positions marked in the SEM image of the LMO-l + LATP pellet sintered at 800 °C for 2 h at a heating rate of 5 K min^{-1} in argon atmosphere.

Table 2 Summary of the results and findings of the analyses of the thermal stability of LMO-l and LATP. DSC Peak positions: 662 °C (P1), 707 °C (P2), 816 °C (P3) and 915 °C (P4)

Detected phases	Valence of transition metals	Temperature range and trend	Possible educts	Possible corresponding DSC peaks	Expected oxygen formation and mass loss	Final composition (wt%)
$LiMnO_2$ (LMO-l)	Mn^{3+}	Decrease already <500 °C, disappearance at 650 °C	—	—	—	—
$Li_{1.3}Al_{0.3}$-$Ti_{1.7}(PO_4)_3$ (LATP)	Al^{3+} and Ti^{4+}	Decrease starts at 525 °C, disappearance at 800 °C	—	—	—	—
$LiMn_2O_4$ (LMO-s)	Mn^{3+} and Mn^{4+}	Detectable between 500 °C and 675 °C	LMO-l	—	No	—
Mn_3O_4	Mn^{2+} and Mn^{3+}	Formation already <500 °C Strong increase up to 700 °C, afterwards steady decrease to 1000 °C, during cooling constant	LMO-l and LMO-s	P1	Yes	3
Li_3PO_4	—	Strong increase to 700 °C strong decrease between 875 °C heating and 875 °C cooling, than increase	LATP	—	No	18
TiO_2	Ti^{4+}	Detectable during heating and cooling	LATP	—	No	—
$LiTiOPO_4$	Ti^{4+}	Detectable between 675 °C and 850 °C	LATP	—	No	—
$LiMnPO_4$	Mn^{2+}	Formation at 500 °C increase between 675 °C and 875 °C decrease between 875 °C heating and 875 °C cooling, than increase	Mn_3O_4 and $LiTiOPO_4$, LATP and during cooling: M–PO_4	P3	Yes	38
$MnTiO_3$	Mn^{2+} and Ti^{4+} + Al^{3+} (dissolved)	Formation at 700 °C strong increase to 950 °C	Mn_3O_4 and $LiTiOPO_4$, TiO_2	P2 and P3	Yes	30
$Li(Mn,Ti)_2O_4$	Mn^{3+} and Ti^{4+} + Al^{3+} (dissolved)	Formation at 575 °C strong increase to 1000 °C	Mn_3O_4, LMO-s and LATP, TiO_2, $LiTiOPO_4$	P1 and P3	Yes (at P1)	11
Cristobalite phase M–PO_4	n/a	Detectable between 875 °C heating and 875 °C cooling	Mn_3O_4, $MnTiO_3$, $LiMnPO_4$ and Li_3PO_4	P4	No	—

Mn_3O_4 (Mn^{2+} and Mn^{3+}) to LMP (Mn^{2+}) and $MnTiO_3$ (Mn^{2+}). The fourth endothermic peak at 915 °C (Fig. 4a, P4) can be correlated to the formation of the cristobalite phase, since no significant mass loss can be detected above 900 °C. Finally, the total mass loss of the LMO-l and LATP powder mixture is 5.2%. The oxygen gassing and decomposition processes cause a porous microstructure with grains of a few 100 nm to 1 μm (Fig. 4b). The EDS analysis (Fig. 4c) confirms the results obtained from HT-XRD measurements. The first position corresponding to the regions with light contrast (Fig. 4b, Pos 1) can be correlated to Mn_3O_4. The second contrast (Fig. 4b, Pos 2) consist of the elements Mn, Ti, O and traces of Al. This can be correlated to $Li(Mn,Ti)_2O_4$ or $MnTiO_3$, in which Al is dissolved. Since Li is below the resolution limit of EDS measurements, a reliable quantitative analysis of the element ratios, and so a separation of $Li(Mn,Ti)_2O_4$ and $MnTiO_3$, is not possible. The further positions 3 and 4 (Fig. 4b) are correlated to LMP and Li_3PO_4.

Comparable to the LMO-s and LATP powder mixture, LMO-l and LATP decomposes below 500 °C, which is accompanied by the reduction of Mn and oxygen gassing. Consequently, this powder mixture is thermally not stable. The findings of this section are summarized in Table 2.

Thermal stability of the LMP and LATP powder mixture

The Rietveld refinements of the XRD diffractograms (Fig. S5, ESI†) reveal a good thermal stability of the LMP and LATP powder mixture. The only additional phase detected corresponds to the oxy-phosphate $LiTiOPO_4$. Its formation starts at 680 °C and its amount increases to 7 wt%, which goes along with the decreases of LMP and LATP by 2 wt% and 5 wt%, respectively (Fig. 5). This reaction correlates to an exothermic peak at 777 °C (Fig. 6a, P1) detected in the DSC measurement. The exothermic peak at 872 °C (Fig. 6a, P2) indicates that the decomposition of the powder mixture takes place above the maximum temperature of the HT-XRD measurement. The final composition after annealing at 800 °C consists of 36 wt% LATP, 57 wt% LMP and 7 wt% $LiTiOPO_4$ (Table 3). No further Mn-containing phase can be detected, which indicates that both LMP and LATP take part in the formation of the oxy-phosphate. That suggest the substitution of two Li^+ by Mn^{2+} or the substitution of Ti^{4+} by Mn^{4+}, which lead to the chemical formulas $Li_{1-x}Mn_{x/2}TiOPO_4$ or $LiMn_{1-y}Ti_yOPO_4$. The general possibility of a Li^+ substitution by Mn^{2+} has been reported for the materials $LiMnPO_4$ and $LiMnVO_4$.[26,27] However, the quantitative analysis of the amounts of substances result in a formation of 0.105 mmol of the oxy-phosphate, which is equal to 7 wt% (12.5 mg) of the 250 mg pellet. The reduction of 2 wt% LMP and 5 wt% LATP equate to 0.032 mmol Mn and 0.055 mmol Ti, which is in total 0.087 mmol, thus, lower than the required amount for the oxy-phosphate formation. That leads to the assumption, that additional Mn- and Ti-containing impurities must be present. Furthermore, the O/P ratio of 5 for

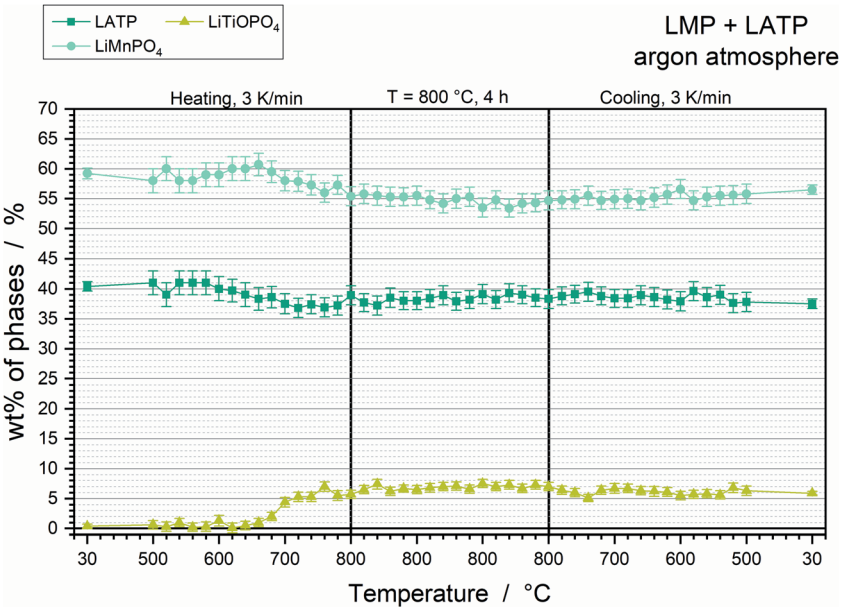

Fig. 5 Phase fractions in wt% of the crystalline phases obtained by Rietveld refinement of the LMP + LATP pellet as a function of the annealing temperature. Heating up to 800 °C with 3 K min^{-1}, holding step at 800 °C for 4 h, and afterwards cooling with 3 K min^{-1} to 30 °C.

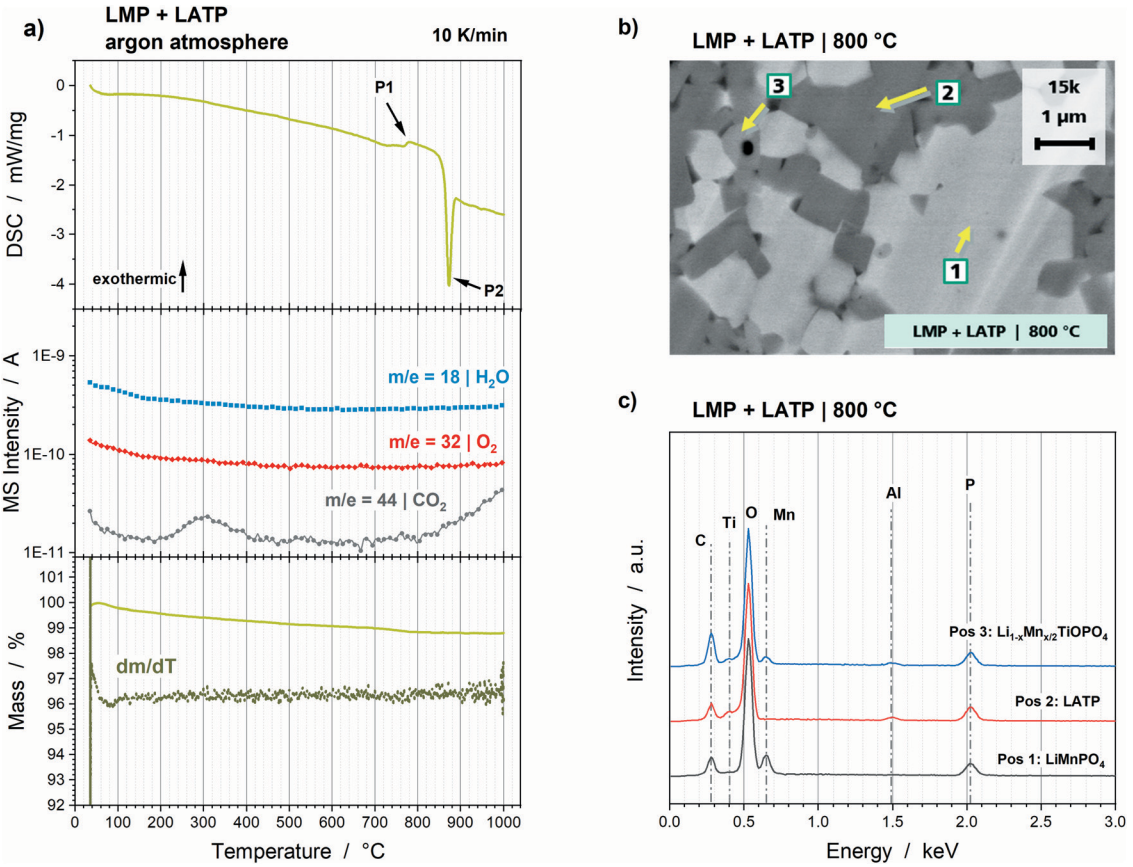

Fig. 6 (a) Results of DSC–TG and MS analyses of a 1 : 1 vol% LMP + LATP powder mixture measured in argon atmosphere with 10 K min^{-1}. (b) SEM cross section and (c) corresponding EDS analyses of the three positions marked in the SEM image of the LMP + LATP pellet sintered at 800 °C for 2 h at a heating rate of 5 K min^{-1} in argon atmosphere.

Table 3 Summary of the results and findings of the analyses of the thermal stability of LMP and LATP. DSC Peak positions: 777 °C (P1) and 872 °C (P2)

Detected phases	Valence of transition metals	Temperature range and trend	Possible educts	Possible corres-ponding DSC peaks	Expected oxygen formation and mass loss	Final composition (wt%)
$LiMnPO_4$ (LMP)	Mn^{2+}	Decrease of 2 wt% at 680 °C, afterwards constant	—	—	—	57
$Li_{1.3}Al_{0.3}Ti_{1.7}(PO_4)_3$ (LATP)	Al^{3+} and Ti^{4+}	Decrease of 5 wt% at 680 °C, afterwards constant	—	—	—	36
$Li_{1-x}Mn_{x/2}TiOPO_4$	Mn^{2+} and Ti^{4+}	Increase to 7 wt% at 680 °C, afterwards constant	LATP, LMP and probably carbonates	P1	No	7

$Li_{1-x}Mn_{x/2}TiOPO_4$ differ from the O/P ratio of 4 for LMP and LATP. That indicates the existence of an additional oxide source, which must provide 1.7 mg O^{2-} (*ca.* 0.7 wt% of 250 mg pellet) for the formation of 0.105 mmol $Li_{1-x}Mn_{x/2}TiOPO_4$ or $LiMn_{1-y}Ti_yOPO_4$. However, the TG analysis of the powder mixture does not show an increase of the total mass, so that incorporation of O_2 impurities from the surrounding argon atmosphere can be excluded. Consequently, the oxidation of the Mn^{2+} to Mn^{4+} for the $LiMn_{1-y}Ti_yOPO_4$ formation is not possible, so that this oxy-phosphate species is highly unlikely. However, a total decrease of 1.2 wt% due to CO_2 formation (Fig. 6a). CO_2 gassing might be caused by the decomposition of carbon containing species, such as Li_2CO_3 or $MnCO_3$, which can be formed during storage[28,29] or are residues of the sol–gel synthesis due to stoichiometric imbalances. The simplified formulations of these reactions show that these carbonates can be the additional source of Mn and O:

$$Li_2CO_3 \rightarrow 2Li^+ + O^{2-} + CO_2\uparrow \text{ or } MnCO_3 \rightarrow Mn^{2+} + O^{2-} + CO_2\uparrow$$

However, this hypothesis has to be tested and verified in further studies by optimizing the synthesis route in order to achieve higher purities of the starting powders. By that a further enhancement of the thermal stability might be achieved, since the reaction of the oxy-phosphate can be probably inhibited without an additional oxygen source. Nevertheless, the thermal stability of the LMP and LATP powder mixture presented here might be sufficient for battery application. Additionally, the SEM cross sections show a very dense microstructure with grains of *ca.* 0.2 μm to *ca.* 2 μm (Fig. 6b), which means a high electrochemical active contact area and short diffusion path ways for Li ions within the grains. The EDS analysis reveal the segregation of the oxy-phosphate in the triple points of the LMP and LATP grains (Fig. 6c, Pos 3). It is not detectable at the direct interface of two grains, so that a drawback for the Li ion charge transfer is not expected.

Thermal stability of the LMP and LATP powder mixture incl. Ag

The LMP and LATP powder mixture showed the most promising thermal stability. Consequently, Ag was added as electrical conductive component, which is necessary for functional bulk cathodes. The XRD patterns before and after annealing up to 800 °C (Fig. 7) show no additional crystalline phase except the expected oxy-phosphate $Li_{1-x}Mn_{x/2}TiOPO_4$. Consequently, Ag has no influence on the thermal stability of the LMP and LATP

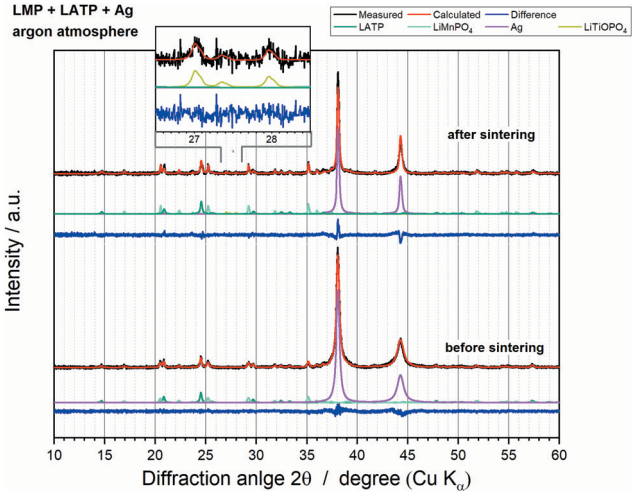

Fig. 7 HT-XRD patterns and their Rietveld refinements of the LMP + LATP + Ag pellet measured at RT before and after sintering in argon atmosphere at 800 °C for 4 h with a heating and cooling rate of 3 K min^{-1}.

powder mixture. However, the analysis of the phase fractions by means of the Rietveld refinements cannot be reliably done, since the absorption coefficient of Ag significantly changes with the increase in particle size from 48–78 nm to *ca.* 2–8 μm (Fig. 8b), which results in an error-prone quantification. Additionally, a high saturation vapour pressure is reported for Ag at 800 °C, so that evaporation of Ag can be assumed during the holding step, which might bias the phase fraction results.[30,31] A more detailed consideration can be found in the ESI† (Fig. S6).

The DSC curve shows two endothermic peaks at 879 °C and 962 °C (Fig. 8a, P1 and P2). The first peak correlates to the decomposition of the LMP and LATP powder mixture (Fig. 6a, P2). The second peak is in accordance with the melting point of the nano particulate Ag powder reported in the data sheet.[32] The TG analysis shows a significant mass loss of 4.7 wt% between 200 °C and 400 °C, which is accompanied by the gassing of CO_2 and several $C_xH_yO_z$ species in the mass to charge ratio range of m/z = 40 to m/z = 87 observable in the MS data. That is caused by the combustion of the carbon coating of the Ag nano particles, necessary to prevent agglomeration and surface oxidation after manufacturing. The combustion is confirmed by the DSC–TG incl. MS measurements of the pure Ag powder (Fig. S7, ESI†). The gassing of the carbon-containing species result in a slightly increased porosity of the pellet

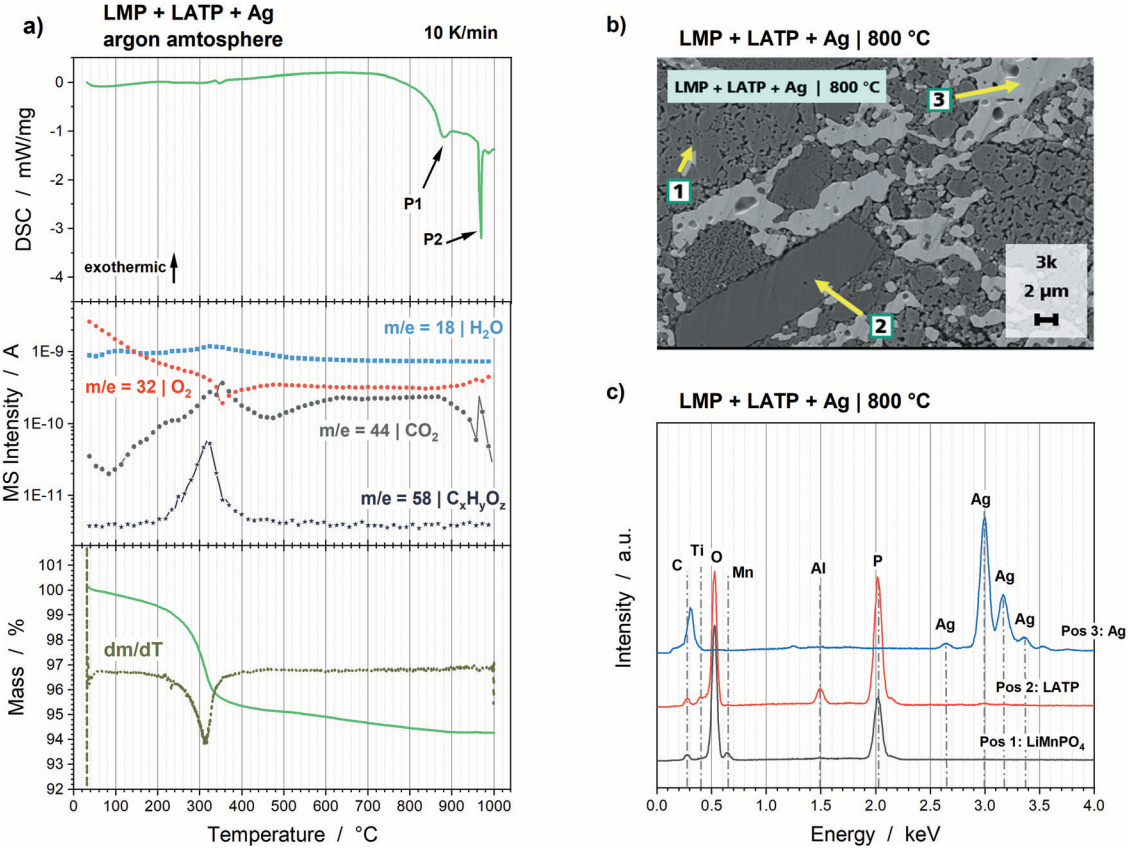

Fig. 8 (a) Results of DSC–TG and MS analyses of a 1 : 1 : 1 vol% LMP + LATP + Ag powder mixture measured in argon atmosphere with 10 K min^{-1}. (b) SEM cross section and (c) corresponding EDS analyses of the three positions marked in the SEM image of the LMP + LATP + Ag pellet sintered at 800 °C for 2 h at a heating rate of 5 K min^{-1} in argon atmosphere. EDS energies for Ag are in accordance with literature.[33]

(Fig. 8b) compared to the LMP + LATP pellet (Fig. 6b). The EDS analyses of the three components show no detectable interdiffusion (Fig. 8c).

Discussion

The spinel LMO-s and layered LMO-l AMs show a comparable behaviour during annealing in combination with LATP. LMO-s and LMO-l decompose intrinsically to mainly Mn_3O_4 already below 500 °C and both vanish at 650 °C. LATP decomposes to TiO_2, Li_3PO_4 and $LiTiOPO_4$ and disappears at 800 °C in both samples. The degradation products are the educts of further reactions to LMP, $MnTiO_3$ and $Li(Mn,Ti)_2O_4$. The driving forces of these reactions are the reduction of the Mn transition metal and the parallel oxidation of O^{2-} to O_2. The oxidation state of Mn changes from 3+ and 4+ for LMO-s or 3+ for LMO-l to 2+ and 3+ for Mn_3O_4 and 2+ for LMP and $MnTiO_3$. The oxygen gassing makes the decomposition thermodynamically more favourable due to a significant increase in entropy. Additionally, the porous microstructure due to the gassing is unusable for bulk cathode application.

In contrast, the oxidation state of Mn in LMP with olivine type structure is 2+. Consequently, a further reduction is not possible. Additionally, the strong covalent bonding within the polyanion PO_4^{3-} inhibits significantly the oxygen formation. Consequently, the LMP and LATP combination is to a high degree thermally stable. The only detected mixed phase is the oxy-phosphate $Li_{1-x}Mn_{x/2}TiOPO_4$. However, its formation at 680 °C is most likely intensified by the decomposition of carbonates, such as Li_2CO_3 or $MnCO_3$, which might be left from synthesis or formed during storage. They work as additional Mn and O source needed for the oxy-phosphate formation. The microstructure appears very dense, since no oxygen gassing takes place.

The addition of Ag as electrical conductive component to the LMP and LATP powder mixture shows no impact on the thermal stability, since no additional phases and no interdiffusion can be detected. The only two drawbacks are the particle growth of the Ag particles and the combustion of their carbon coating, which result in a slightly more porous microstructure compared to the LMP and LATP pellet. Overall, this material combination seem to be a promising candidate towards ASSB bulk cathodes.

Conclusion

The investigation of the thermal stabilities of the three Mn-based AMs LMO-s, LMO-l and LMP in combination with

the ceramic solid-state electrolyte LATP reveal that the 1 : 1 vol% powder mixture of LMP and LATP remain to a high degree thermally stable after sintering at 800 °C in argon atmosphere. The addition of Ag particles as electrical conductor has no influence on the thermal stability. In contrast, the LMO-s and LMO-l AMs decompose in combination with LATP, which is driven by Mn reduction and oxygen formation. As long as these reactions cannot be suppressed, LMO-l and LMO-s are not useable in ceramic ASSB bulk cathodes.

Conclusively, the LMP, LATP and Ag combination can be a good starting point for further investigation on the optimizations of the composition and sintering process, which should be validated by electrochemical measurements. Percolation and tortuosity need to be considered by choosing the ratio as well as particle sizes for AM, SSE and electrical conductor.

Conflicts of interest

The authors declare no conflict of interest. The funders had no role in the design of the study; in the collection, analyses, or interpretation of data; in the writing of the manuscript, or in the decision to publish the results.

Acknowledgements

The authors acknowledge the financial support from the Bavarian Ministry of Economic Affairs and Media, Energy and Technology for funding the Fraunhofer R&D Center for Electromobility Bavaria FZEB (Grant number: 43-6629/86).

References

1 W. Hou, X. Guo, X. Shen, K. Amine, H. Yu and J. Lu, *Nano Energy*, 2018, **52**, 279–291.
2 Y.-S. Hu, *Nat. Energy*, 2016, **1**, 652.
3 J. Janek and W. G. Zeier, *Nat. Energy*, 2016, **1**, 1167.
4 A. C. Luntz, J. Voss and K. Reuter, *J. Phys. Chem. Lett.*, 2015, **6**, 4599–4604.
5 D. H. S. Tan, A. Banerjee, Z. Chen and Y. S. Meng, *Nat. Nanotechnol.*, 2020, **15**, 170–180.
6 R. C. Xu, X. H. Xia, S. Z. Zhang, D. Xie, X. L. Wang and J. P. Tu, *Electrochim. Acta*, 2018, **284**, 177–187.
7 T. Zhang, W. He, W. Zhang, T. Wang, P. Li, Z. Sun and X. Yu, *Chem. Sci.*, 2020, **334**, 928.
8 F. Zheng, M. Kotobuki, S. Song, M. O. Lai and L. Lu, *J. Power Sources*, 2018, **389**, 198–213.
9 J. Li, C. Ma, M. Chi, C. Liang and N. J. Dudney, *Adv. Energy Mater.*, 2015, **5**, 1401408.
10 M. Gellert, E. Dashjav, D. Grüner, Q. Ma and F. Tietz, *Ionics*, 2018, **24**, 1001–1006.
11 L. Miara, A. Windmüller, C.-L. Tsai, W. D. Richards, Q. Ma, S. Uhlenbruck, O. Guillon and G. Ceder, *ACS Appl. Mater. Interfaces*, 2016, **8**, 26842–26850.
12 J. Sastre, X. Chen, A. Aribia, A. N. Tiwari and Y. E. Romanyuk, *ACS Appl. Mater. Interfaces*, 2020, 36196–36207.
13 P. Hofmann, F. Walther, M. Rohnke, J. Sann, W. G. Zeier and J. Janek, *Solid State Ionics*, 2019, **342**, 115054.
14 C. B. Carter and M. G. Norton, *Ceramic materials. Science and engineering*, Springer, New York, 2007.
15 Q. Jiang and Z. Wen, *Thermodynamics of materials*, Higher Education Press/Springer-Verlag, Beijing, Heidelberg, 2011.
16 B. V. L′vov, *Thermal decomposition of solids and melts. New thermochemical approach to the mechanism, kinetics, and methodology*, Springer, New York, 2007.
17 C. M. Julien, A. Mauger, K. Zaghib and H. Groult, *Inorganics*, 2014, **2**, 132–154.
18 N. Nitta, F. Wu, J. T. Lee and G. Yushin, *Mater. Today*, 2015, **18**, 252–264.
19 A. K. Padhi, K. S. Nanjundaswamy and J. B. Goodenough, *J. Electrochem. Soc.*, 1997, **144**, 1188–1194.
20 K. Nanjundaswamy, *Solid State Ionics*, 1996, **92**, 1–10.
21 Y. Ren, K. Chen, R. Chen, T. Liu, Y. Zhang and C.-W. Nan, *J. Am. Ceram. Soc.*, 2015, **98**, 3603–3623.
22 A. R. Armstrong and P. G. Bruce, *Nature*, 1996, **381**, 499–500.
23 Y. J. Gu, Y. B. Chen, H. K. Wu, X. W. Huang, X. B. Liu, H. Z. Cui, Y. M. Wang, Z. N. Yang, C. L. Wang and H. Huo, *Key Eng. Mater.*, 2008, **368-372**, 270–273.
24 I. M. Kötschau and J. R. Dahn, *J. Electrochem. Soc.*, 1998, **145**, 2672–2677.
25 A. Manthiram, *Nat. Commun.*, 2020, **11**, 1550.
26 O. Clemens, R. Haberkorn and H. P. Beck, *J. Solid State Chem.*, 2011, **184**, 2640–2647.
27 O. Clemens, R. Haberkorn, M. Springborg and H. P. Beck, *Z. Anorg. Allg. Chem.*, 2014, **640**, 173–183.
28 B. Ammundsen, P. B. Aitchison, G. R. Burns, D. J. Jones and J. Rozière, *Solid State Ionics*, 1997, **97**, 269–276.
29 I. A. Shkrob, J. A. Gilbert, P. J. Phillips, R. Klie, R. T. Haasch, J. Bareño and D. P. Abraham, *J. Electrochem. Soc.*, 2017, **164**, A1489–A1498.
30 M. Ohring, *Materials science of thin films. Deposition and structure*, Academic Press, San Diego, CA, 2nd edn, 2002.
31 H. M. Schadel and C. E. Birchenall, *JOM*, 1950, **2**, 1134–1138.
32 Nanografi, Ag(silver) Nanoparticles 48–78 nm, Safety Data Sheet, 2017.
33 N. A. N. Mohamad, N. A. Arham, J. Junaidah, A. Hadi and S. A. Idris, *IOP Conf. Ser.: Mater. Sci. Eng.*, 2018, **358**, 12063.